

Received March 23, 2022, accepted May 12, 2022, date of publication May 17, 2022, date of current version June 3, 2022.

Digital Object Identifier 10.1109/ACCESS.2022.3175880

Improved Resonant Converter for Dynamic Wireless Power Transfer Employing a Floating-Frequency Switching Algorithm and an Optimized Coil Shape

SHAHRIAR SARMAST GHOHFAROKHI¹, HADI TARZAMNI^{1,2}, (Student Member, IEEE), FARZAD TAHAMI¹, (Senior Member, IEEE), AND JORMA KYRYA², (Member, IEEE)

¹Department of Electrical Engineering, Sharif University of Technology, Tehran 1456717368, Iran

²Department of Electrical Engineering and Automation, Aalto University, 02150 Espoo, Finland

Corresponding author: Farzad Tahami (tahami@sharif.edu)

This work was supported by Finnish Electronic Library (FinELib), Finland, under the FinELib Consortium's Agreement with IEEE.

ABSTRACT This paper offers a new EF-class converter for dynamic wireless power transfer application. The proposed high-frequency converter employs a floating-frequency switching algorithm to control the converter in a continuous frequency range, eliminate the requirement to any additional operational data from the secondary (receiver) side, accelerate the load impedance match while moving, maximize the transferred power rate, reduce charging interval and compensate power transfer tolerances. Moreover, an optimized super elliptical shape coil is designed to cope with lateral misalignment, enhance coil coupling, and increase efficiency. In the proposed converter, (i) soft switching is implemented to increase switching frequency, decrease passive components size, and improve power density, (ii) undesired voltage harmonics are attenuated to reduce peak voltage stress of the power switch in a wide frequency range, (iii) the receiver side is enabled for higher mobility with stable power transfer, and (iv) the resonant frequency is updated to compensate non-accurate values of passive components in experimental prototyping. In this study, the operational analytics, compensation method, control algorithm, coil design and converter optimization are followed with some comparisons to present the converter capabilities. In addition, simulation and experimental results are provided under different degrees of misalignment to verify the accuracy of theoretical analytics.

INDEX TERMS EF-class resonant converter, floating-frequency switching algorithm, coil shape optimization, dynamic wireless power transfer.

I. INTRODUCTION

With wide applications in electrical vehicles [1], medical devices [2], robotics [3], and mobile phones [4], wireless power transfer (WPT) is becoming an emphatic, growingly-dominant and controversial issue in industry. This challenging power transfer method provides isolation between source and load ports, prevents connector fatigue, diminishes over-dependence on the charging battery, presents more flexibility, and improves the reliability rate in undesirable environmental conditions [5]. Meanwhile, coil coupling, operation in misalignment, parasitic components, topology and coil shape design, power transfer rate, charge duration, and receiver-side

data transfer have been the main issues to be researched and improved in recent years [6]. In [7], the effect of misalignment tolerance has been analyzed on the transferred power and output voltage of an inductive WPT resonant converter where different compensation methods have been tested. Other recent studies have investigated the efficiency improvement of the WPT technique by co-implementing of inductive and capacitive methods [8], cascading a buck-boost converter [9], optimizing driver operation [10], utilizing a series-parallel resonant coupling [11], and adding an intermediate coil [12]. Moreover, a multi-phase parallel inverter and a parallel LCL topology have been used in [13], [14], respectively, to enhance the transferred power.

Dynamic wireless power transfer (DWPT) is one of the emerging subject matters in industrial and research fields,

The associate editor coordinating the review of this manuscript and approving it for publication was Zhuang Xu¹.

which presents some additional features, such as charging interval, installed battery size, weight and cost reduction. Moreover, it can improve battery life [15]. In [16], a converter has been introduced for DWPT with mutual inductance (MI) estimation in misalignment. However, low switching frequency has increased its coil size. In [17], a resonant converter utilizing a φ_2 class inverter has been presented to reduce input current ripple where the obtained efficiency is low. The suggested converter in [18] has concentrated the control algorithm improvement by utilizing an active rectifier for simultaneous implementation of a phase-locked loop and a chained trigger mode, which has led to a complicated control system. In [19], a multi-phase WPT converter has been presented. Although it has been aimed to improve transferred power rate, employing a high number of semiconductors has restricted industrial applications of [19]. The presented converter in [20] has tried to accomplish a higher power transfer rate in DWPT by integrating a two-layer receiver-side coil; meanwhile, using four resonant tanks with series compensation has increased the system weight. In [21], different compensation approaches have been evaluated in a DWPT converter to decrease load voltage sensitivity in misaligned conditions. In addition, detailed analytics of a resonant WPT converter with series-series compensation and using a dq synchronous reference frame model have been provided in [22]. The literature [23] has aimed to compensate coupling factor changes in a DWPT converter by employing an active variable reactance rectifier. The main drawbacks of [23] are the requirement for a secondary control system and operation under a fixed frequency. In [24]–[26], the effects of a series/series-parallel compensation tank, ferrite core geometry and resonant frequency mismatch have been evaluated on the efficiency and output voltage of the DWPT system. The suggested converter in [27] has concentrated on solving the current imbalance problem of a WPT system with a high order resonant tank. Nevertheless, the accessibility requirement of sender and receiver ports for control implementation has restricted its applicability. In [28], a new topology for WPT has been introduced to widen loading conditions where high number of passive and active components has reduced its efficiency. The main aim of [29] is to suggest a soft switching inverter with WPT application; however, load and MI changes, misalignment, and frequency modulation have not been considered. The literature [30] has proposed a new multi-phase structure for WPT. Although using a multi-phase rectifier has improved the power transfer rate, poor coil coupling has limited the application of [30] in low power implementation. In [31], a maximum efficiency point tracking algorithm has been suggested for a DWPT converter where the wireless communication between the sender and receiver has increased cost and restricted its application in noisy environments.

In this paper, a new resonant converter is proposed for the DWPT application where its main contribution can be categorized in: (i) a new topology to reduce switch voltage stress and attenuate undesired voltage harmonics,

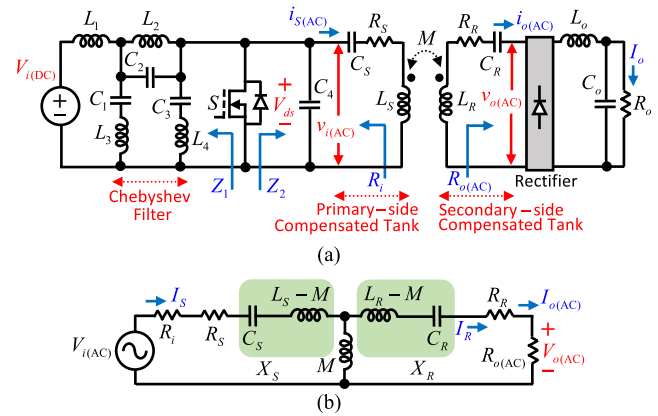


FIGURE 1. Proposed converter. (a) Detailed topology illustration with instant value labels. (b) T-model of the simplified topology with phasor labels.

(ii) an optimized coil shape to improve dynamic coil coupling, cope with misalignment and enhance power density, and (iii) a floating-frequency switching algorithm with receiver-side data estimation to accelerate the load impedance match while moving, maximize the transferred power rate, reduce charging interval, and compensate power transfer tolerances. The main application of the proposed converter is in the wireless charging system of low power robotic carriers. The rest of this paper is organized as follows: In Section II, the proposed DWPT topology is introduced. Section III is devoted to the converter operation features and optimized design. Section IV presents the implemented floating-frequency switching algorithm. Comprehensive optimized-coil design and operation are provided in Section V which are followed by the experimental results of a 0.8kW prototype in Section VI, and the conclusion in Section VII.

II. PROPOSED RESONANT CONVERTER

The proposed resonant DWPT converter for the robotic carrier's application is shown in Fig. 1(a), which consists of an input DC supply, a Chebyshev filter, a single switch (S) inverter, primary- and secondary-side compensated resonant tanks, a WPT coil, a receiver-side rectifier, output filter (L_o) and output load (R_o). The WPT coil is modeled through a sender (L_S) and a receiver (L_R) self-inductance, and a mutual inductance (M). Moreover, R_S , R_R , C_S and C_R are the internal coil resistances and compensation capacitors, respectively. In this topology, a series-series compensation is employed in the sender-receiver sides, which provides higher efficiency, simpler analytics, and easier control than other compensation approaches [18], [22]. The T-model of the simplified topology for first harmonic with components reflection to the AC side is depicted in Fig. 1(b) which leads to, (1), as shown at the bottom of the next page.

In (1), $\omega = 2\pi f$ is the angular switching frequency, and $R_o(\text{AC}) = (\pi^2/8)R_o$ and $I_o(\text{AC}) = (2/\pi)I_o$ are vivid with the receiver-side full-bridge diode rectifier. Furthermore, voltage

equations of the resonant tank components are calculated as

$$V_{CS} = -j \frac{I_S}{C_S \omega}, \quad V_{CR} = -j \frac{I_R}{C_R \omega}, \quad (2)$$

$$V_{LS} = jL_S \omega I_S - jM \omega I_R, \quad V_{LR} = jL_R \omega I_R + jM \omega I_S. \quad (3)$$

III. CONVERTER OPERATION FEATURES

A. OPTIMIZED TOPOLOGY DESIGN

The coupling factor between the sender and receiver coils is defined as follows:

$$k = M / \sqrt{L_S L_R}. \quad (4)$$

Unlike transformers with constant k values close to the unit, k equals much lower values in DWPT systems. Moreover, due to the permanent misalignment of coils while moving, M and consequently k are variable. The main aim of the proposed DWPT converter is to improve k , which is equivalent to transferring higher portion of energy from the sender to the receiver coil, and preventing energy storage in the coils leakage inductances. Considering $X = X_S = X_R$ and ignoring R_i , R_S and R_R in Fig. 1(b), output power of the proposed converter is given by

$$P_o = \frac{R_{o(AC)} V_{i(AC)}^2}{\left| jX \left(2 + \frac{X}{M\omega} \right) + R_{o(AC)} \left(1 + \frac{X}{M\omega} \right) \right|^2}. \quad (5)$$

In order to maximize P_o with regards to the tank design, $dP_o/dX = 0$ should be satisfied, which results in $X = 0$ or $-2M\omega$. In other words, X_S and X_R should be simultaneously equal to zero to improve k values to the unit which can be summarized as

$$(L_S - M)\omega = 1/C_S \omega, \quad (L_R - M)\omega = 1/C_R \omega. \quad (6)$$

With variable values of M , (6) leads to $L_S = L_R$ and $C_S = C_R$. Therefore, the primary- and secondary-side tanks parameters should be designed the same to obtain optimized power transfer.

Based on Fig. 1(b), equation of the converter efficiency is concluded as follows:

$$\eta = \frac{R_{o(AC)}}{R_{o(AC)} + R_R + (R_i + R_S) \frac{(X+M\omega)^2 + (R_R + R_{o(AC)})^2}{(M\omega)^2}}. \quad (7)$$

By ignoring R_S and R_R , and full compensation of X_S and X_R , (7) can be simplified as

$$\eta = \frac{R_{o(AC)}}{R_{o(AC)} + R_i \frac{(M\omega)^2 + R_{o(AC)}^2}{(M\omega)^2}}. \quad (8)$$

Solving $d\eta/dX = 0$, the maximum efficiency of the proposed converter is realized in $X = -M\omega$; and according

to (8), $M\omega \gg R_{o(AC)}$ results in higher efficiency. Hence, the converter should be designed with higher frequency range to enhance η . In addition, the higher M facilitates $M\omega \gg R_{o(AC)}$ which is more probable in highly-aligned coil conditions.

From another viewpoint, if lower sensitivity of P_o and η with regards to load change is aimed, $dP_o/dR_{o(AC)} = 0$ and $d\eta/dR_{o(AC)} = 0$ lead to (9) and (10), respectively.

$$R_{o(AC)} = R_R + M^2 \omega^2 / R_S \quad (9)$$

$$R_{o(AC)} = \sqrt{R_R^2 + M^2 \omega^2 R_R / R_S} \quad (10)$$

Since $M^2 \omega^2 \gg R_S, R_R$, then $R_{o(AC)}$ for maximum P_o in (9) is higher than the corresponding $R_{o(AC)}$ for maximum η in (10). Therefore, $X = 0$ and close values of $M\omega$ and $R_{o(AC)}$ result in low sensitivity of P_o and η with regards to $R_{o(AC)}$ variation, respectively.

As evaluated in this section, optimization of P_o and η , or reduction of P_o and η sensitivities with respect to $R_{o(AC)}$ contribute to different design and operation conditions. In other words, simultaneous optimization of these factors is unfeasible. In this paper, optimization of P_o under acceptable η is focused, which is suitable for battery size and charging time reduction.

B. CHEBYSHEV FILTER DESIGN

According to the misalignment, variable M , and the requirement of load impedance matching to maximize the transferred power rate, the proposed DWPT converter should operate with floating frequency. Therefore, main features of the converter should be achievable in a wide frequency spectrum. In this paper, a Chebyshev filter is implemented in the primary side of the proposed converter which presents (i) higher attenuation rate than Butterworth and Bessel filters, and (ii) less sensitivity to the passive components values than Elliptical filters. This band rejection filter should be designed to attenuate the 2nd-order harmonic of f which satisfies lower switch voltage stress and soft switching in S . In this case, the DWPT converter becomes capable to operate with higher input voltage and power transfer rate. In addition, various families of power switches with low drain-to-source resistances and higher switching frequencies can be utilized as S which facilitates the manufacturing procedure. Based on the filter design rules in [32] and the attenuation profile of a band rejection filter in Fig. 2, the filter bandwidth proportion is defined as

$$\frac{BW_C}{BW} = \frac{f_4 - f_1}{f_3 - f_2} \quad (11)$$

where, BW_C and BW are the corresponding 3dB and desired attenuation bandwidth, respectively. In this paper,

$$\begin{bmatrix} R_i + R_S + j \left(L_S \omega - \frac{1}{C_S \omega} \right) & -jM\omega \\ -jM\omega & R_R + R_{o(AC)} + j \left(L_R \omega - \frac{1}{C_R \omega} \right) \end{bmatrix} \times \begin{bmatrix} I_S \\ I_R \end{bmatrix} = \begin{bmatrix} V_{i(AC)} \\ 0 \end{bmatrix} \quad (1)$$

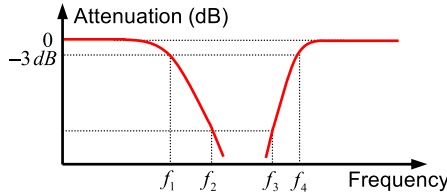


FIGURE 2. Attenuation profile of a band rejection filter.



FIGURE 3. Normalized switch voltage stress of [33] with the switching frequency of $f - 7.5\%$.

$BW_C/BW = 2$ is selected where the desired attenuation of $20dB$ and considering the bandwidth ripple of $1dB$ result in a 3rd-order Chebyshev filter in Fig. 1(a). The filter components are designed based on (12) for parallel and (13) for series resonant tanks [32].

$$C_1 = C_3 = \frac{C_n}{2\pi R_{o(AC)} BW_C}, \quad L_3 = L_4 = \frac{R_{o(AC)} BW_C}{2\pi f_0^2 L_n}, \quad (12)$$

$$C_2 = \frac{BW_C}{2\pi f_0^2 R_{o(AC)} C_n}, \quad L_2 = \frac{R_{o(AC)} L_n}{2\pi BW_C} \quad (13)$$

where, C_n , L_n and $f_0 = 2f$ are the normalized capacitor and inductor, and the cutoff frequency of the Chebyshev filter. They are equal to $C_n = 2.216$ and $L_n = 1.088$ for the initial design assumption of this paper [32]. Furthermore, the input inductor of the proposed converter is calculated as

$$L_1 = \frac{1}{9\pi^2 f^2 C_4} \quad (14)$$

C. SWITCH VOLTAGE STRESS

In some previous literature, switch voltage stress decrease is concentrated where the presented ϕ_2 class converter in [33] is one of the most successful candidates. That converter comes up with the switch voltage stress of $2V_{i(DC)}$ to $2.5V_{i(DC)}$ which provides higher input voltage, power density, and switching frequency capabilities. Meanwhile, narrow band rejection spectrum restricts the applicability of [33] in DWPT systems with high misalignment tolerance. This drawback is expressed in Fig. 3 where all features—i.e., low switch voltage stress and soft switching—are lost in a little frequency variation of $f - 7.5\%$. In order to cope with misalignment and floating frequency, the proposed converter presents a wider band rejection spectrum, which is demonstrated with the seen impedance magnitude evaluation of switch ($Z_{ds} = Z_1 \parallel Z_2$)

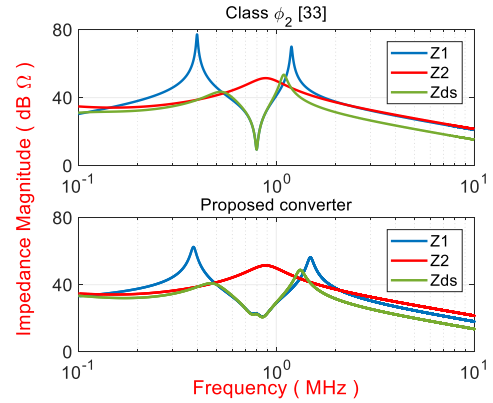


FIGURE 4. Seen impedance magnitude comparison of switch in the proposed and ϕ_2 class converter.

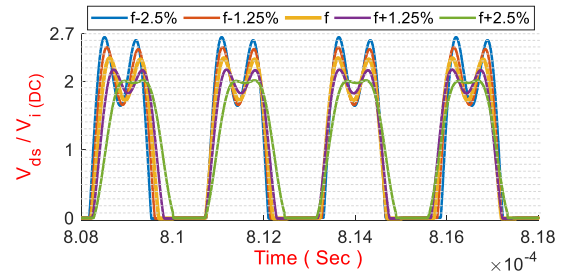


FIGURE 5. Normalized switch voltage stress of the proposed converter in different switching frequency values.

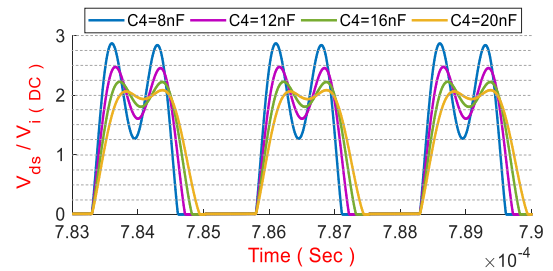


FIGURE 6. Normalized switch voltage stress of the proposed converter in different C_4 values.

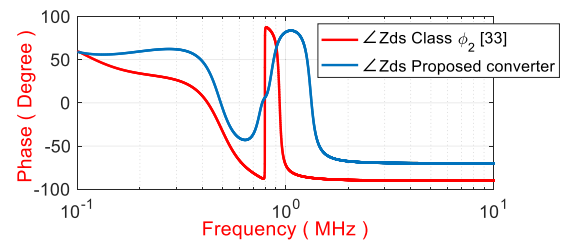


FIGURE 7. Seen phase comparison of switch in the proposed and ϕ_2 class converter.

in Fig. 4. In this figure, $f = 400 kHz$ is considered for the same operational characteristics of the proposed and ϕ_2 class converter, and the results verify that $|Z_{ds}|$ of the proposed converter is attenuated in a wider band around $2f$ with

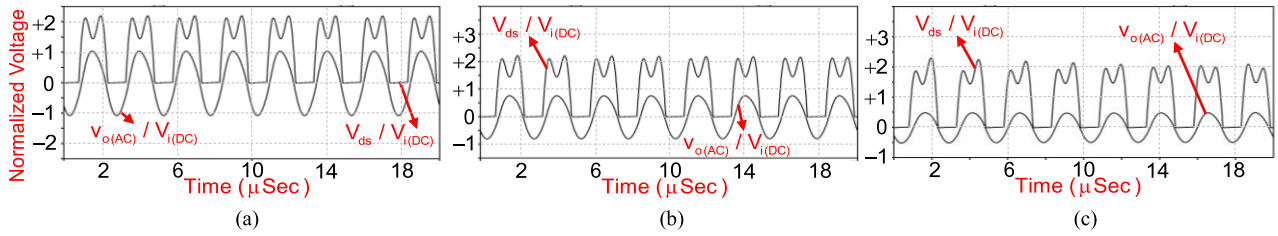


FIGURE 8. Normalized switch voltage stress and output voltage of the φ_2 class converter without the output rectifier. (a) $k = 0.2$. (b) $k = 0.15$. (c) $k = 0.1$.

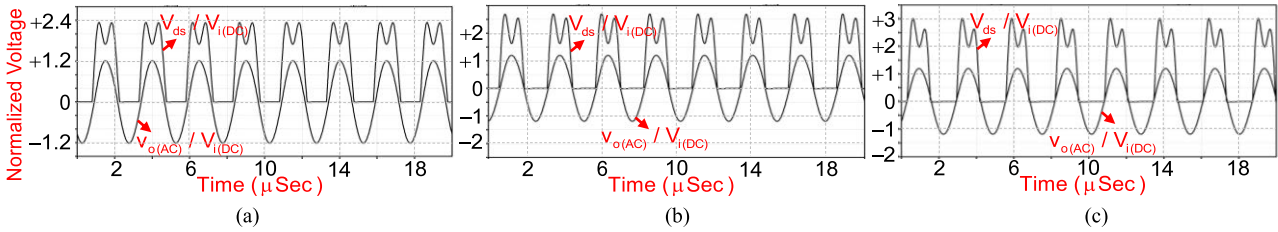


FIGURE 9. Normalized switch voltage stress and output voltage of the proposed converter without the output rectifier. (a) $k = 0.2$. (b) $k = 0.15$. (c) $k = 0.1$.

less attenuation ripple, which satisfies lower switch voltage stress. Moreover, in Fig. 5, the normalized switch voltage stress ($V_{ds}/V_{i(DC)}$) of the proposed converter is evaluated with regards to f variation, and the results highlight the 2nd-order harmonic attenuation (low switch voltage stress) in different switching frequency values.

As depicted in Fig. 1(a), capacitor C_4 is placed in parallel with S which can be either the parasitic capacitance of S , or a separate external capacitor. Attenuation of $|Z_{ds}|$ in the 3rd-order harmonic is the main role of C_4 , and it should be designed large enough to present acceptable attenuation. The effect of C_4 on the switch voltage stress is shown in Fig. 6.

D. ZERO VOLTAGE SWITCHING

High switching frequency, high power density and low resonant tank size are the capabilities satisfied through soft switching condition. As compared in Fig. 7, zero voltage switching (ZVS) is achieved in a wider switching frequency band for the proposed converter than the φ_2 class converter. Note that the lagging phase of $\angle Z_{ds}$ provides ZVS condition for S ($\angle Z_{ds} > 0$). In order to finalize the proposed converter capabilities verification, normalized $v_{o(AC)}$ and V_{ds} values of the φ_2 class and the proposed converter are compared in Fig. 8 and Fig. 9, respectively. According to this comparison, which is performed for different k values, the proposed converter (i) presents more pure sinusoidal voltage waveform for $v_{o(AC)}$, (ii) transfers more power to the receiver side in k variation, (iii) provides more stable $v_{o(AC)}$ in a wider frequency spectrum, and (iv) has lower normalized switch voltage stress with respect to the transferred voltage ($V_{ds}/v_{o(AC)}^{\max}$) especially in lower k values.

IV. VARIABLE FREQUENCY CONTROL STRATEGY

Inaccessibility of receiver-side control signals in the primary side, due to the lack of feedback control loop, is the main

challenge in the control procedure of a WPT system. In some previous literature, wireless signal communication is introduced to develop a closed loop feedback from the receiver to the sender side [27], [34] and [35]. Meanwhile, complicated control system, various environmental conditions and noise of the environment or the WPT converter restrict wireless signal communication applicability. These obstacles are highlighted in DWPT systems due to permanent misalignment of coils. In this paper, a simple control algorithm based on the receiver-side data estimation is presented to overcome the aforementioned obstacles (see Fig. 10). Considering the operation conditions of DWPT, some initial requirements should be satisfied. For instance, a coil-embedded road is necessary for electrical vehicles DWPT where the data of the load and receiver-side coil/compensator (based on vehicles standard design) are detected in the beginning of the road to pay the charges. With this sensible assumption and without any additional measured data from the receiver side, the proposed method estimates the receiver-side load current ($I_{R(k)}$) and MI ($M(k)$) in each algorithm iteration (k) by

$$I_{R(k)} = \sqrt{\frac{(R_i + R_S + L_S s + (1/C_S s))I_{S(k)}^2 - V_{i(AC)}I_{S(k)}}{R_R + R_{o(AC)} + L_R s + (1/C_R s)}}, \quad (15)$$

$$M(k) = \frac{(\frac{R_R + R_{o(AC)}}{s} + L_R - \frac{1}{C_R s^2})I_{R(k)}}{I_{S(k)} - I_{R(k)}}. \quad (16)$$

In the preceding equations, R_S , L_S and $I_{S(k)}$ are available in the sender side and $s = j\omega(k)$. As shown in Fig. 10, the converter starts with an initial f and then by measuring $V_{i(AC)}$ and I_S , the value of $M(k)$ is calculated with (15) and (16). By considering P_o optimization, $\omega_{(k+1)}$ is obtained from (6), and based on the estimated output power value, f is increased or decreased which reflects the increment or reduction of M , respectively. Eventually, by reducing $M(f)$, the alignment of

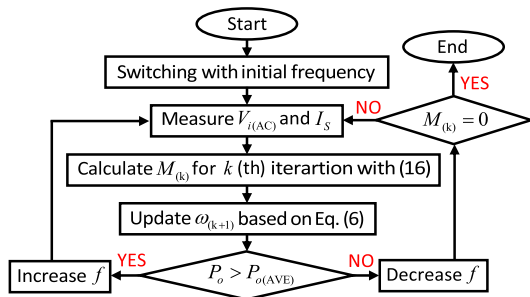


FIGURE 10. Control diagram of the DWPT system based on receiver-side data estimation.

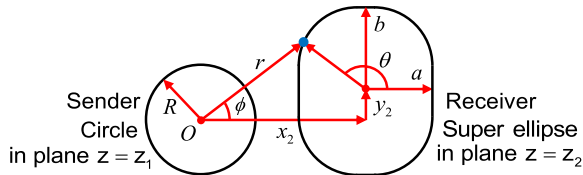


FIGURE 11. Sender and receiver coils shape and location.

sender and receiver coils decreases to zero and the control loop ends. Using this control algorithm helps to (i) faster dynamic response and load impedance match due to less measurements and data transfer, (ii) shorter charging interval, (iii) better resonant tank compensation, (iv) effective operation in noisy environments and (iv) higher power transfer rate while moving.

V. COIL FORMULATION, DESIGN AND OPERATION

Misalignment is inevitable in DWPT; hence, designing suitable resonant tank coils to satisfy the desired features alongside with misalignment is a challenging issue. Transferring high power in the fully aligned condition is the main characteristic of circular coils. However, MI decreases sharply in the misalignment. On the other hand, rectangular coils present lower MI with less sensitivity to the misalignment. This paper aims to propose the aforementioned features simultaneously. Therefore, the receiver coil is considered to be a super ellipse and the formulations are presented for the generalized shape conditions. Fig. 11 illustrates the location and shape of the sender (circle) and receiver (super ellipse) coils considering misalignment where the circle and super ellipse are centered at $(x, y, z) = (0, 0, z_1)$ and (x_2, y_2, z_2) , respectively. In addition, y_2 and x_2 are the longitudinal and lateral misalignments, respectively.

As discussed in Section III Part A, the higher $M\omega$, the more transferred power rate. In this case, coil shape does not have any effect on the ω values; meanwhile, it plays a determinative role in coils coupling. Therefore, MI can be considered as a metric to evaluate the capability of the coils in power transferring. Equations of magnetic potential (A) and MI of the depicted coils system in Fig. 11 are equal to [36]

$$A_\phi(R, r, z - z_1) = \frac{\mu_0 I_S R}{2} \int_0^\infty J_1(sR) J_1(sr) \exp(-s|z - z_1|) ds \quad (17)$$

TABLE 1. Normalized MI in lateral misalignment.

n	q	$\hat{M} \times 10^6$ in $R = 0.5 m$, $ z_2 - z_1 = 0.15 m$ and $a = b = 0.2 m$				
		$x_2 = 0$	$x_2 = 0.05$	$x_2 = 0.10$	$x_2 = 0.15$	$x_2 = 0.20$
2	1.256	1.1884	1.1828	1.1689	1.1310	1.0666
2.5	1.311	1.2373	1.2317	1.2133	1.1771	1.1078
3	1.355	1.2604	1.2494	1.2296	1.1932	1.1213
3.5	1.392	1.2565	1.2501	1.2307	1.1971	1.1202
4	1.424	1.2480	1.2454	1.2427	1.2055	1.1112

$$A_r = A_\phi(R, r, z - z_1) e_\phi \quad (18)$$

$$M = \oint_C A_r \cdot dr \quad (19)$$

where, J_1 , μ_0 , e_ϕ and C are Bessel function of the first kind of order one, vacuum permeability coefficient, unit vector and integral closed loop path of the receiver coil, respectively. For a general super elliptical coil centered at (x_2, y_2, z_2) , C is defined as

$$C \triangleq \begin{cases} x(\theta) = x_2 + a \cos^{2/n} \theta \\ y(\theta) = y_2 + b \sin^{2/n} \theta \end{cases} \quad (20)$$

where, n is the order (curve coefficient) of a super ellipse in the cylindrical coordinate system, and $n = 2$ leads to a circle (if $a = b$) or a simple ellipse (if $a \neq b$). Moreover, $n \rightarrow \infty$ results in a square (if $a = b$) or a rectangle (if $a \neq b$). Hence, the MI equation in the cylindrical coordinate system is concluded as

$$M = \frac{\mu_0 R}{2} \int_0^\infty \int_0^{2\pi} \frac{J_1(sR) J_1(sr(\theta)) \Psi(\theta) \exp(-s|z - z_1|)}{nr(\theta)} d\theta ds \quad (21)$$

where,

$$r(\theta) = \sqrt{(x_2 + a \cos^{2/n} \theta)^2 + (y_2 + b \sin^{2/n} \theta)^2} \quad (22)$$

$$\Psi(\theta) = 2 \csc \theta \sec \theta [a \sin^2 \theta \cos^{2/n} \theta (b \sin^{2/n} \theta + y_2) + b \cos^2 \theta \sin^{2/n} \theta (a \cos^{2/n} \theta + x_2)] \quad (23)$$

In order to take the impact of misalignment into account, the below-curve area of M in the whole range where two coils face each other is defined as

$$\hat{M} \triangleq \int_{-\infty}^{+\infty} M dy/q \quad (24)$$

In (24), q is the perimeter of receiver coil which is utilized to normalize the MI with regards to the coil size.

$$q = 4 \int_0^{\pi/2} \sqrt{\rho + \left(\frac{d\sqrt{\rho}}{d\theta}\right)^2} d\theta \quad (25)$$

$$\rho = (a \cos^{2/n} \theta)^2 + (b \sin^{2/n} \theta)^2 \quad (26)$$

To evaluate effect of the parameters in Fig. 11 and achieve the optimized receiver coil shape, (21) is plotted under different conditions and \hat{M} is calculated for each plot in Fig. 12.

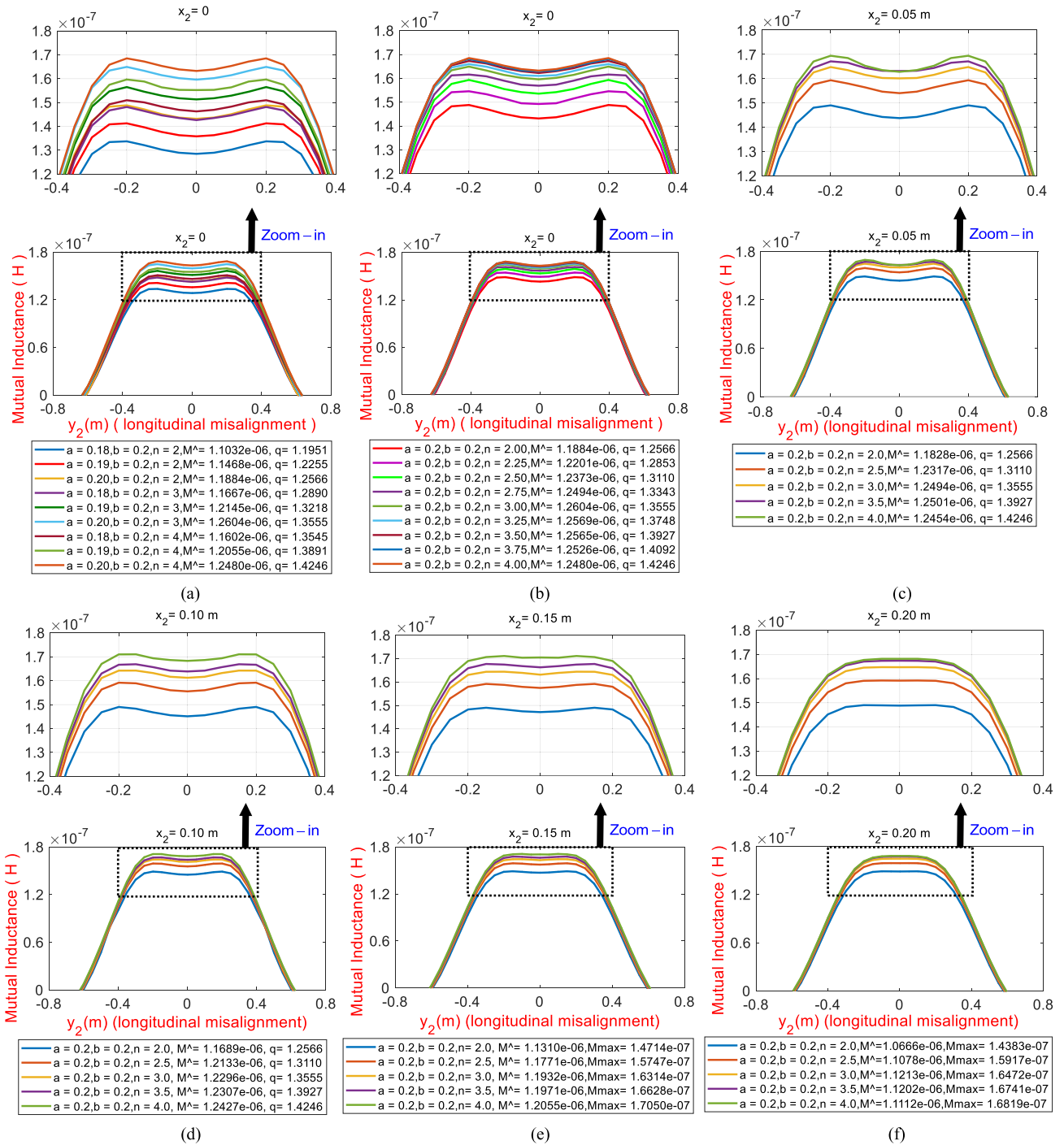


FIGURE 12. Mutual inductance with respect to longitudinal misalignment in $R = 0.5\text{ m}$, $|z_2 - z_1| = 0.15\text{ m}$: (a) a variation in $x_2 = 0$. (b) n variation in $x_2 = 0$. (c) n variation in $x_2 = 0.05\text{ m}$. (d) n variation in $x_2 = 0.1\text{ m}$. (e) n variation in $x_2 = 0.15\text{ m}$. (f) n variation in $x_2 = 0.2\text{ m}$.

In Fig. 12(a), “ b ” is considered constant and the effect of “ a ” variation is tested in different “ n .” The outcome verifies that $a = b$ presents the highest \hat{M} in all “ n ”; therefore, it is selected as the best solution for the super ellipse semi-axes. Moreover, it is clear that the super ellipse ($n > 2$) owes higher \hat{M} than the corresponding circle ($n = 2$) with the same diameter, which is reflected in the \hat{M} improvement of 6% and

5% in $n = 3$ and $n = 4$, respectively. This is the result of better coil coupling in the super ellipse than the circle during misalignment.

The next step is to select “ n ” which is assessed in Figs. 12(b)-(f) and Table 1. In Figs. 12(b)-(f), MI and \hat{M} are calculated with different x_2 , and “ n ” varies in each figure where $n = 3$ and $n = 3.5$ present the best feature. In this

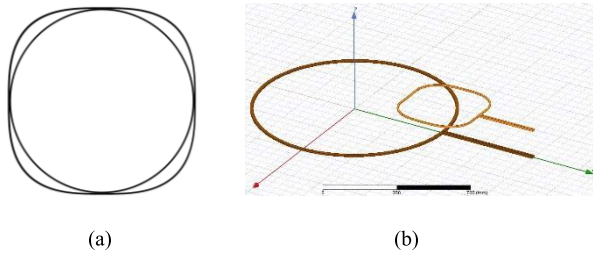


FIGURE 13. Super ellipse geometry. (a) Comparison of a circle and a super ellipse ($n = 3$) with the same diameter. (b) Finite element simulation topology.

paper, $n = 3$ is selected for the receiver coil because: (i) it leads to lower coil copper (weight) than $n = 3.5$, and (ii) it provides better coil coupling around laterally-aligned condition with higher power transfer. The geometrical shape of a super ellipse with $n = 3$ is shown in Fig. 13(a).

Furthermore, the theoretical results of Fig. 12 are validated through some finite element simulations where the geometrical topology of coils and simulation outcome are illustrated in Fig. 13(b) and Fig. 14, respectively. Note that, it is not possible to define a super ellipse in the Maxwell software directly. Therefore, (20) should be modeled through the Taylor series of sinus and cosine functions in $0 \leq \theta \leq \pi/2$ as follows:

$$C \triangleq \begin{cases} x(\theta) = a \times \left(1 - \frac{\theta^2}{2!} + \frac{\theta^4}{4!} - \frac{\theta^6}{6!} + \frac{\theta^8}{8!} - \dots \right)^{2/n} \\ \quad + x_2 \\ y(\theta) = b \times \left(\theta - \frac{\theta^3}{3!} + \frac{\theta^5}{5!} - \frac{\theta^7}{7!} + \frac{\theta^9}{9!} - \dots \right)^{2/n} \\ \quad + y_2 \end{cases} \quad (27)$$

It is clear that the accuracy of the model depends on the number of considered Taylor series terms where four terms are selected in this paper, and the result is satisfactory in Fig. 13(b). As a result of these simulations, the simulated MI plot in Fig. 14(a) verifies the theoretical plot of Fig. 12(a) for $n = 3$ which is tested without ferrite magnetics. In Fig. 14(b), k is depicted with respect to y_2 and as declared, the obtained coupling coefficient is low without ferrite magnetics. Therefore, in order to enhance k and also satisfy the safety issues of industrial chargers, some ferrite magnetics are placed behind each coil, and the result shows considerable improvement of k in Fig. 14(c).

VI. EXPERIMENTAL VERIFICATION

The experimental setup and its components are illustrated in details in Fig. 15. Moreover, the designed values of converter and coils are tabulated in Table 2 where the Chebyshev filter components are designed to attenuate the 2nd order harmonic of switch voltage stress for 20dB. As a practical design consideration, C_S and C_R are implemented by a series-parallel combination of film capacitors to: (i) reduce their equivalent series resistance (ESR), and (ii) tolerate high voltage and

TABLE 2. Experimental prototype specifications.

Component	Specification	Component	Specification
MOSFET	K39n60W	Gate driver	UCC27322P
Opto-coupler	HCPL7720	Op-Amp	LM324
IC power supply	LM2576	Microcontroller	STM32H750VB
C_1, C_3	5.28 nF	C_2	77 nF
C_S, C_R	5.4 nF	L_1 (10 turns)	50 μ H
L_2 (15 turns)	550 nH	L_3, L_4 (7 turns)	7.5 μ H
$z_2 - z_1$	15 cm	n	3
Sender coil	5 turns	Receiver coil	6 turns
R	17.5 cm	$a = b$	13.5 cm
L_S, L_R	20 μ H	Max. M	2 μ H
Misalignment	$0 < x_2 < 14$ cm	Max. k	0.1
Min f	450 kHz	Max f	520 kHz
Nominal P_o	800 W	Max tested P_o	320 W
Nominal $i_{S(AC)}$	8 A	Max tested $i_{S(AC)}$	4.5 A
Nominal $i_{o(AC)}$	8 A	Max tested $i_{o(AC)}$	3.8 A
Max coil efficiency	$\approx 91\%$	Max total efficiency	$\approx 80\%$

current stresses. Instead of utilizing Litz wiring for the coils, they are built with a thicker single-string wire since it presents better forming features in circle and super ellipse shapes. In addition, due to the existence of sufficient air gap in the ferrite-magnet-implemented coils, saturation of ferrite cores is ignored in the design procedure.

Fig. 16 shows the examples of experimental results under different misalignment conditions where $V_{i(DC)} = 70$ V. In Figs. 16(a)-(c), the floating f is equal to 513.9 kHz, 496.8 kHz and 475.1 kHz to cope with the coupling coefficients of $k = 0.1$, $k = 0.05$ and $k = 0.01$, respectively, which verifies the capability of the proposed topology in maximizing the transferred power, accelerating load-impedance match, correct receiver-side load current and MI estimation, low switch voltage stress and coping with misalignment. Fig. 16(a) reflects the converter operation in its maximum MI of 2 μ H where the 2nd-order harmonic of switch voltage stress is attenuated considerably. Moreover, the 3rd-order harmonic of V_{ds} is low by selecting an adequate value for C_4 and ZVS is satisfied. As the main feature expressed in Figs. 16(b) and (c), the proposed converter provides maximum possible power transfer, acceptable power efficiency and ZVS simultaneously, even in the very low coupling coefficient of $k = 0.01$. In Fig. 16(d), the Fast Fourier Transform (FFT) spectrum of V_{ds} is presented, which highlights the 2nd-order harmonic attenuation and low value of the 3rd-order harmonic.

As discussed in Section II, achieving the maximum power transfer and the highest efficiency is not feasible simultaneously. Hence, a strategy is considered in the experimental tests to obtain maximum power transfer with acceptable efficiency. However, higher misalignment values lead to MI, and then efficiency, drop sharply. In this case, in order to prevent low efficiency values, f is adapted with small changes to improve efficiency, which results in little output power decrease. The two- and three-dimensional plots of output power and efficiency with respect to misalignment are shown

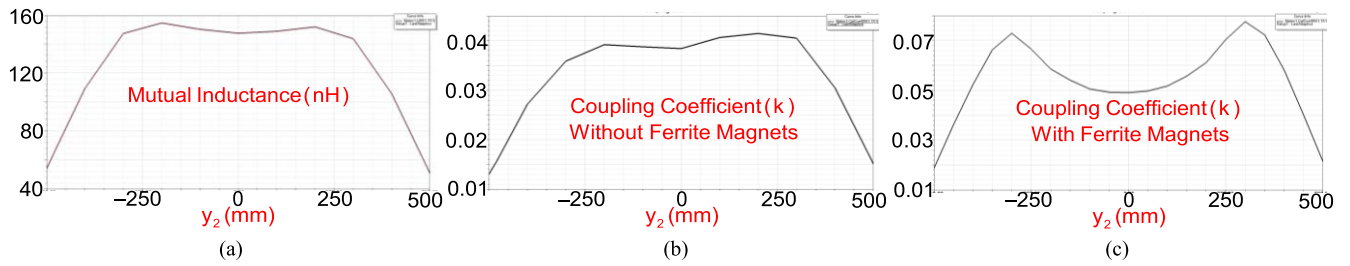


FIGURE 14. Simulation results of a circle sender and a super ellipse receiver. (a) MI without ferrite magnets. (b) k without ferrite magnets. (c) k with ferrite magnets.

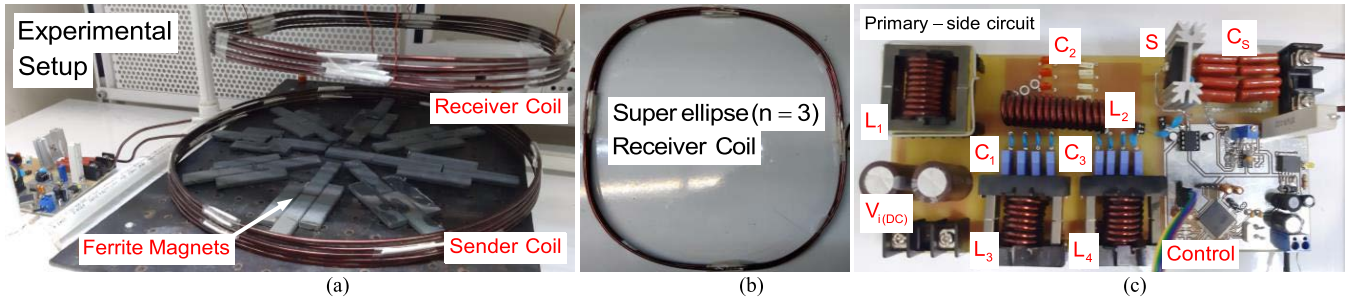


FIGURE 15. Experimental prototype. (a) Setup. (b) Super ellipse ($n = 3$) coil of the receiver side. (c) Primary-side power and control circuit.

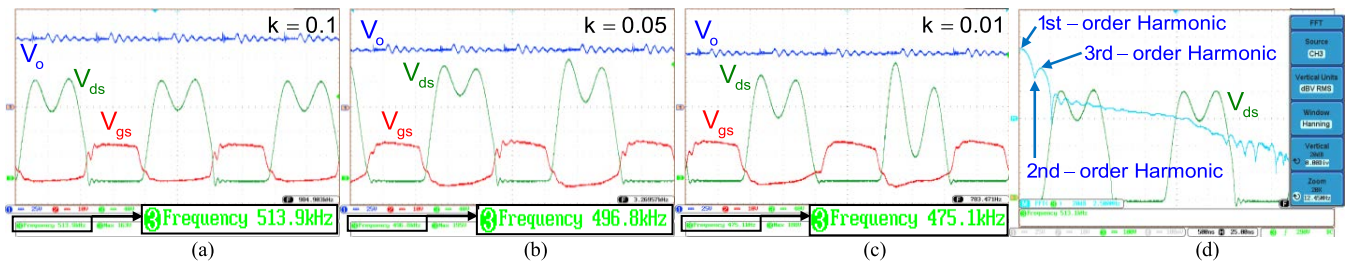


FIGURE 16. Experimental results in different misalignment conditions. (a) $k = 0.1$. (b) $k = 0.05$. (c) $k = 0.01$. (d) FFT spectrum of switch voltage stress.

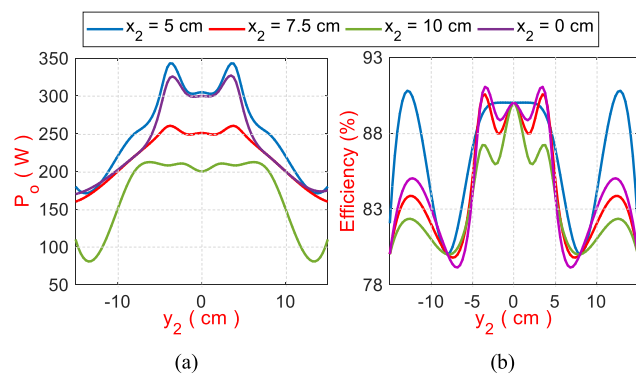


FIGURE 17. Operation characteristics with respect to misalignment. (a) Output power. (b) Efficiency of the resonant tank.

in Fig. 17 and Fig. 18, respectively. As concluded from Fig. 18, the maximum power transfer is achieved in a ring centered at $(x_2, y_2) = (0, 0)$ by implementing the proposed switching algorithm.

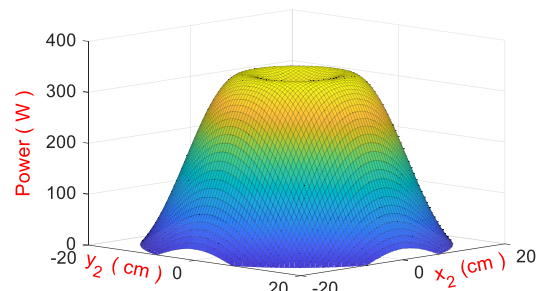


FIGURE 18. Output power with respect to the longitudinal and lateral misalignments.

VII. CONCLUSION

In this paper, a new DWPT converter was proposed for the wireless charging system of the robotic carriers, which focused on improving topology operation characteristics, control strategy and coil shape design. The proposed topology employed a 3rd-order Chebyshev filter in the sender

side to attenuate the switch voltage 2nd-order harmonic in a wider switching frequency spectrum with low attenuation ripple. Moreover, the switch parallel capacitor was designed to attenuate the switch voltage 3rd-order harmonic while providing ZVS condition for the main switch. This condition enabled the proposed converter to operate under high switching frequency, low switching power loss, low passive components size, and high power density. From the control strategy point of view, a floating-frequency switching algorithm was implemented on the proposed converter with no requirement to any load-side data measurement. This simple switching algorithm, which utilized the estimated mutual inductance to regulate the switching frequency, led to faster dynamic response in misalignment, higher mobility of receiver side, better resonant tank compensation, higher power transfer rate while moving, faster charging, and wider industrial applicability of the proposed converter in noisy environments. As one of the significant contributions of this paper, the optimized coils with circle and super ellipse ($n = 3$) shapes in the sender and receiver sides were analyzed, evaluated and designed to achieve maximum power transfer and low sensitivity to the misalignment. The results verified the enhancement of more than 5% in the transferred power of the designed coil than the circular one for various misalignment conditions. In this paper, the design specifications, operation features and comparison outcome were validated through finite element simulation and experimental results.

REFERENCES

- [1] K. T. Chau, *Electric Vehicle Machines and Drives: Design, Analysis and Application*. Hoboken, NJ, USA: Wiley, 2015.
- [2] R. Sedehi, D. Budgett, J. Jiang, and X. Ziyi, "A wireless power method for deeply implanted biomedical devices via capacitively coupled conductive power transfer," *IEEE Trans. Power Electron.*, vol. 36, no. 2, pp. 1870–1882, Feb. 2021.
- [3] J. Wu, X. Dai, R. Gao, and J. Jiang, "A coupling mechanism with multidegree freedom for bidirectional multistage WPT system," *IEEE Trans. Power Electron.*, vol. 36, no. 2, pp. 1376–1387, Feb. 2021.
- [4] M. Huang, Y. Lu, and R. P. Martins, "A reconfigurable bidirectional wireless power transceiver for battery-to-battery wireless charging," *IEEE Trans. Power Electron.*, vol. 34, no. 8, pp. 7745–7753, Aug. 2019.
- [5] Z. Zhang, H. Pang, A. Georgiadis, and C. Cecati, "Wireless power transfer—an overview," *IEEE Trans. Ind. Electron.*, vol. 66, no. 2, pp. 1044–1058, Feb. 2019.
- [6] C. T. Rim and C. Mi, *Wireless Power Transfer for Electric Vehicles and Mobile Devices*. Hoboken, NJ, USA: Wiley, 2017.
- [7] G. Ke, Q. Chen, W. Gao, S.-C. Wong, C. K. Tse, and Z. Zhang, "Research on IPT resonant converters with high misalignment tolerance using multicore receiver set," *IEEE Trans. Power Electron.*, vol. 35, no. 4, pp. 3697–3712, Apr. 2020.
- [8] F. Lu, H. Zhang, H. Hofmann, and C. C. Mi, "An inductive and capacitive combined wireless power transfer system with LC-compensated topology," *IEEE Trans. Power Electron.*, vol. 31, no. 12, pp. 8471–8482, Dec. 2016.
- [9] M. Fu, C. Ma, and X. Zhu, "A cascaded boost-buck converter for high efficiency wireless power transfer systems," *IEEE Trans. Ind. Informat.*, vol. 10, no. 3, pp. 1972–1980, Aug. 2014.
- [10] M. Pinuela, D. C. Yates, S. Lucyszyn, and P. D. Mitcheson, "Maximizing DC-to-load efficiency for inductive power transfer," *IEEE Trans. Power Electron.*, vol. 28, no. 5, pp. 2437–2447, May 2013.
- [11] L. Chen, S. Liu, Y. C. Zhou, and T. J. Cui, "An optimizable circuit structure for high-efficiency wireless power transfer," *IEEE Trans. Ind. Electron.*, vol. 60, no. 1, pp. 339–349, Jan. 2013.
- [12] S. Moon, B.-C. Kim, S.-Y. Cho, C.-H. Ahn, and G.-W. Moon, "Analysis and design of a wireless power transfer system with an intermediate coil for high efficiency," *IEEE Trans. Ind. Electron.*, vol. 61, no. 11, pp. 5861–5870, Nov. 2014.
- [13] Q. Deng, J. Liu, D. Czarkowski, W. Hu, and H. Zhou, "An inductive power transfer system supplied by a multiphase parallel inverter," *IEEE Trans. Ind. Electron.*, vol. 64, no. 9, pp. 7039–7048, Sep. 2017.
- [14] H. Hao, G. A. Covic, and J. T. Boys, "A parallel topology for inductive power transfer power supplies," *IEEE Trans. Power Electron.*, vol. 29, no. 3, pp. 1140–1151, Mar. 2014.
- [15] C. Qiu, "Design, analysis and application of dynamic wireless power transfer," Ph.D. dissertation, School Energy Environ., Univ. Hong Kong, Hong Kong, 2016.
- [16] R. Tavakoli and Z. Pantic, "Analysis, design, and demonstration of a 25-kW dynamic wireless charging system for roadway electric vehicles," *IEEE Trans. Emerg. Sel. Topics Power Electron.*, vol. 6, no. 3, pp. 1378–1393, Sep. 2018.
- [17] J. Choi, W. Liang, L. Raymond, and J. Rivas, "A high-frequency resonant converter based on the class Phi2 inverter for wireless power transfer," in *Proc. IEEE 79th Veh. Technol. Conf. (VTC Spring)*, Seoul, South Korea, May 2014, pp. 1–5.
- [18] Y. Jiang, L. Wang, Y. Wang, M. Wu, Z. Zeng, Y. Liu, and J. Sun, "Phase-locked loop combined with chained trigger mode used for impedance matching in wireless high power transfer," *IEEE Trans. Power Electron.*, vol. 35, no. 4, pp. 4272–4285, Apr. 2020.
- [19] H. Ota, T. Ise, J. Liu, and Y. Miura, "A feasibility study on multi-phase wireless power transfer using frequency modulation," in *Proc. 45th Annu. Conf. IEEE Ind. Electron. Soc. (IECON)*, Lisbon, Portugal, Oct. 2019, pp. 1502–1507.
- [20] N. Xia, Z. Yuan, Y. Zhu, and Y. Wang, "Integrated receiver with high misalignment tolerance used in dynamic wireless charging," *IET Electr. Power Appl.*, vol. 14, no. 10, pp. 1918–1924, Oct. 2020.
- [21] A. Ramezani and M. Narimani, "Optimized electric vehicle wireless chargers with reduced output voltage sensitivity to misalignment," *IEEE J. Emerg. Sel. Topics Power Electron.*, vol. 8, no. 4, pp. 3569–3581, Dec. 2020.
- [22] S. Lee and S.-H. Lee, "dq synchronous reference frame model of a series-series tuned inductive power transfer system," *IEEE Trans. Ind. Electron.*, vol. 67, no. 12, pp. 10325–10334, Dec. 2020.
- [23] S. Sinha, A. Kumar, B. Regensburger, and K. K. Afridi, "Active variable reactance rectifier—A new approach to compensating for coupling variations in wireless power transfer systems," *IEEE J. Emerg. Sel. Topics Power Electron.*, vol. 8, no. 3, pp. 2022–2040, Sep. 2020.
- [24] Z. Huang, Z. Fang, C.-S. Lam, P.-I. Mak, and R. P. Martins, "Design of series/series-parallel compensated inductive power transfer converter as wireless grid to vehicle interface," in *Proc. IEEE Vehicle Power Propuls. Conf. (VPPC)*, Hanoi, Vietnam, Oct. 2019, pp. 1–5.
- [25] E. A. Elghanam, H. H. Kaban, M. S. Hassan, and A. Osman, "Design and modeling of ferrite core geometry for inductive wireless chargers of electric vehicles," in *Proc. Int. Conf. Electr. Comput. Technol. Appl. (ICECTA)*, Ras Al Khaimah, United Arab Emirates, Nov. 2019, pp. 1–5.
- [26] H. Weerasekara, K. Hata, T. Imura, and Y. Hori, "Effect of resonance frequency mismatch for transmission power in wireless power transfer system," in *Proc. IEEE Vehicle Power Propuls. Conf. (VPPC)*, Hanoi, Vietnam, Oct. 2019, pp. 1–4.
- [27] Y. Li, J. Hu, X. Li, F. Chen, Q. Xu, R. Mai, and Z. He, "Analysis, design, and experimental verification of a mixed high-order compensations-based WPT system with constant current outputs for driving multistring LEDs," *IEEE Trans. Ind. Electron.*, vol. 67, no. 1, pp. 203–213, Jan. 2020.
- [28] G. R. Kalra, D. J. Thrimawithana, B. S. Riar, C.-Y. Huang, and M. Neuburger, "A novel boost active bridge-based inductive power transfer system," *IEEE Trans. Ind. Electron.*, vol. 67, no. 2, pp. 1103–1112, Feb. 2020.
- [29] H. Tebianian, Y. Salami, B. Jeyasurya, and J. E. Quaicoe, "A 13.56-MHz full-bridge class-D ZVS inverter with dynamic dead-time control for wireless power transfer systems," *IEEE Trans. Ind. Electron.*, vol. 67, no. 2, pp. 1487–1497, Feb. 2020.
- [30] J. Lim, B. Lee, and M. Ghovanloo, "A multiphase resonance-based boosting rectifier with dual outputs for wireless power transmission," *IEEE Trans. Power Electron.*, vol. 35, no. 3, pp. 2680–2689, Mar. 2020.
- [31] W. Zhang, X. Wu, C. Xia, and X. Liu, "Maximum efficiency point tracking control method for series-series compensated wireless power transfer system," *IET Power Electron.*, vol. 12, no. 10, pp. 2534–2542, Aug. 2019.

- [32] C. Bowick, *RF Circuit Design*, 2nd ed. Boston, MA, USA: Newnes, 2008.
- [33] J. M. Rivas, Y. Han, O. Leitermann, A. D. Sagneri, and D. J. Perreault, "A high-frequency resonant inverter topology with low-voltage stress," *IEEE Trans. Power Electron.*, vol. 23, no. 4, pp. 1759–1771, Jul. 2008.
- [34] N. Khan, H. Matsumoto, and O. Trescases, "Wireless electric vehicle charger with electromagnetic coil-based position correction using impedance and resonant frequency detection," *IEEE Trans. Power Electron.*, vol. 35, no. 8, pp. 7873–7883, Aug. 2020.
- [35] Y. Li, J. Hu, X. Li, R. Mai, Z. Li, M. Liu, and Z. He, "Efficiency analysis and optimization control for input-parallel output-series wireless power transfer systems," *IEEE Trans. Power Electron.*, vol. 35, no. 1, pp. 1074–1085, Jan. 2020.
- [36] J. T. Conway, "Exact solutions for the mutual inductance of circular coils and elliptic coils," *IEEE Trans. Magn.*, vol. 48, no. 1, pp. 81–94, Jan. 2012.



SHAHRIAR SARMAST GHOHFAROKHI was born in Esfahan, Iran, in 1994. He received the B.Sc. and M.Sc. degrees in electronics engineering and power electronics engineering from the Department of Electrical Engineering, Sharif University of Technology, Tehran, Iran, in 2018 and 2020, respectively. His research interests include power electronics, wireless power transfer, AC–DC micro-grids, and renewable energies.



HADI TARZAMNI (Student Member, IEEE) was born in Tabriz, Iran, in 1992. He received the B.Sc. and M.Sc. degrees (Hons.) in power electrical engineering from the Faculty of Electrical and Computer Engineering, University of Tabriz, Tabriz, in 2014 and 2016, respectively. He is currently pursuing the Ph.D. degree in power electronics engineering with the Department of Electrical Engineering, Sharif University of Technology, Tehran, Iran, and the Department of Electrical Engineering and Automation, Aalto University, Finland, under the Dual-Degree Doctoral Program. Since January 2021, he has been a Researcher at the Department of Electrical Engineering and Automation and the Department of Electronics and Nanoengineering, Aalto University. He has authored and coauthored more than 25 journals and conference papers. He also holds six patents in the area of power electronics. His research interests include power electronic converters analysis and design, DC–DC and DC–AC converters, high step-up power conversion, soft-switching and resonant converters, and reliability analysis. He was a recipient of the Best Paper Award in Tenth International Power Electronics, Drive Systems and Technologies Conference (PEDSTC), in 2019. He has received a three-year Aalto ELEC Doctoral School Grant, in 2021.



FARZAD TAHAMI (Senior Member, IEEE) received the B.S. degree in electrical engineering from the Ferdowsi University of Mashhad, Mashhad, Iran, in 1991, and the M.S. and Ph.D. degrees in electrical engineering from the University of Tehran, Tehran, Iran, in 1993 and 2003, respectively. From 1991 to 2004, he was with the Research and Development Department, Jovain Electrical Machines Corporation (JEMCO), Iran. In 2004, he joined the Sharif University of Technology, Tehran, where he is currently an Associate Professor. His current research interests include electric motor drives, modeling and control of power electronic converters, soft switching, resonant converters, high-frequency power conversion, and wireless power transfer. Since 2007, he has been the Chairperson of the Technical Committee of Rotating Machinery and the Iranian National Electrotechnical Committee (INEC). He is a member of the Board of Directors and the Chairman of the Education Committee of the Power Electronics Society of Iran (PESI).



JORMA KYRA (Member, IEEE) received the M.Sc., Lic.Sc., and D.Sc. degrees from the Helsinki University of Technology (TKK), which is now Aalto University, Helsinki, Finland, in 1987, 1991, and 1995, respectively. Since 1985, he has been with the university in various positions. Since 1996, he has been an Associate Professor of power electronics. Since 1998, he has been a Professor of power electronics. From 2008 to 2009, he was the Dean of the Faculty of Electronics, Communications and Automation, TKK. From 2009 to 2011, he was the Vice President of Aalto University, Espoo, Finland. He is currently the Head of the Department of Electrical Engineering and Automation, Aalto University. His research interest includes power electronics at large. The power electronics group at Aalto University has expertise, such as in power electronics for ac drives, dc–dc converters, modeling of converters, filtering of EMI, power factor correction, and distributed power systems.

...